

Dipolar spin relaxation of divacancy qubits in silicon carbide

Oscar Bulancea Lindvall,¹ Nguyen Tien Son,¹ Igor A. Abrikosov,¹ and Viktor Ivády^{1,2,*}

¹*Department of Physics, Chemistry and Biology,
Linköping University, SE-581 83 Linköping, Sweden*

²*Wigner Research Centre for Physics,
PO Box 49, H-1525, Budapest, Hungary*

(Dated: February 4, 2021)

Abstract

Divacancy spins in silicon carbide implement qubits with outstanding characteristics and capabilities, including but not limited to, 64 ms coherence time, spin-to-photon interfacing, and sizable, 10% – 30% room-temperature read-out contrast, all of these in an industrial semiconductor host. Despite these great demonstrations, there are still numerous open questions on the physics of divacancy point defects. In particular, spin relaxation, which sets the fundamental limit for the spin coherence time, has not been thoroughly studied yet. Here, we carry out theoretical simulations of environmental spin induced spin relaxation processes of different divacancy configurations in 4H-SiC. We reveal magnetic field values where the longitudinal spin relaxation time T_1 drops resonantly due to the coupling to either ^{29}Si and ^{13}C nuclear spins or electron spins associated with other defects and dopants. We quantitatively analyze the dependence of the T_1 time on the concentration of the defect spins and the applied magnetic field in the most relevant cases and provide a simple analytical expression allowing either for estimation of the T_1 time in samples with known spin defect concentration or for estimation of the local spin defect concentration of an ensemble or a single divacancy qubit from the measured relaxation rates.

I. INTRODUCTION

Through the example of the nitrogen-vacancy center in diamond¹⁻⁴ (NV center), point defects in wide-band gap semiconductors have demonstrated their potential for quantum-enhanced technologies. In particular, the NV center based devices are about to revolutionize sensing at the nanometer scale⁵⁻¹², while NV centers coupled to adjacent nuclear spins can serve as nodes for quantum internet¹³⁻¹⁵ and quantum computations¹⁶⁻¹⁸. While the physics of the NV center is understood to a very large degree, other point defect qubits with similar or even superior capabilities, such as the neutral silicon and carbon vacancy pair (divacancy)¹⁹⁻²¹ and the negatively charged silicon vacancy (silicon vacancy)^{22,23} in silicon carbide (SiC) are still subjects of active fundamental studies. For example, recent reports on the neutral divacancy have demonstrated 64 ms coherence time²⁴, implementation of spin-to-photon interface²⁵, nuclear spin operations for quantum memory applications^{26,27}, and a room temperature spin contrast as high as 30%²⁸. The fact that SiC is a technologically mature semiconductor with controllable p- and n-type doping and established nanofabrication techniques further enhances its importance and paves the way toward affordable integrated quantum devices²⁹⁻³¹.

Besides coherent properties of the qubits, longitudinal spin relaxation, with the corresponding decay time T_1 , is of great importance as it sets the fundamental limit for several applications, e.g. for dynamic decoupling techniques and sensing.³²⁻³⁵ Relaxation of the NV center's electron spin at different magnetic fields, temperatures, and environmental spin defect concentration has been studied.^{36,37} Furthermore, optical signatures of strong environmental couplings were revealed, enabling novel microwave free spectroscopy applications.³⁸⁻⁴² In contrast, much less is known about the longitudinal spin relaxation of divacancy qubits in SiC. The T_1 time was reported for specific values of the magnetic field at various temperatures⁴³⁻⁴⁵, however, no systematic studies on the environmental couplings and resulting spin relaxation processes have been carried out yet. Even less is known about environmental resonances that may give rise to T_1 spectroscopy and dynamic nuclear polarization in SiC.

In semiconductors, there are two main contributions to the spin relaxation dynamics of point defect qubits. Phonon assisted processes are dominating the temperature dependence and the high temperature region of the spin relaxation. On the other hand, spin flip-flop and spin precession due to the environmental spins are most important at low temperatures and at high spin concentrations. The latter may be critical for shallow defects in nanometer scale sensing applications and

for integrated devices, where spin relaxation may enhance due to the increased doping level. Coupling to defects with various local spin Hamiltonians give rise to a rich phenomena with numerous resonances where the spin relaxation rate can be enhanced by several orders of magnitude.⁴⁶ Recent developments in point defect spin dynamics simulations have made theoretical spin relaxation studies possible, even in *ab initio* manner.^{46,47}

In this article, we study the longitudinal spin relaxation of divacancy qubits in 4H-SiC due to various environmental spins, such as spin-1/2, spin-1, and spin-3/2 point defects and ¹³C and ²⁹Si nuclear spins. First, we identify the most relevant resonance magnetic field values where efficient coupling to the environmental spins leads to enhanced spin relaxation, and second, we quantitatively study the spin relaxation rate, T_1^{-1} , over a wide range of magnetic field values, two orders of magnitude variation of the defect concentration, and various isotope abundances. We provide a simple analytical formula with theoretically fitted constants that can be used to obtain ensemble averaged T_1 time in a sample of given defect concentration and isotope abundance.

The paper is organized as follows. Sec. II discusses divacancy and majority spin defects in SiC. In Sec. III, we describe the numerical methods utilized in our study. Sec. IV collects our results on resonant spin mixing due to various environmental spins (Sec. IV A) and on longitudinal spin relaxation due to nuclear spins and spin-1/2 defects (Sec. IV B). In Sec. V, we summarize our findings.

II. BACKGROUND

Silicon carbide is a polytypic material with the 4H polytype being the most stable⁴⁸ and most commonly used one. The primitive cell of 4H-SiC consists of four Si-C double layers in hexagonal stacking order. Due to the stacking of the double layers, there are two non-equivalent positions for single site point defects in 4H-SiC. The next nearest neighbor sites of the so-called *h* and *k* defect sites show hexagonal-like and cubic-like local arrangements, respectively. In a perfect 4H-SiC lattice, the divacancy, as an adjacent pair of vacancies, has four distinguishable configurations *hh*, *kk*, *hk*, and *kh*, where the first and second letter indicate the carbon and silicon vacancy sites, respectively. These configurations in the above specified order were assigned⁴⁹ to the PL1, PL2, PL3, and PL4 photoluminescence (PL) signals⁴³, respectively. Here, we note that there are additional divacancy related PL lines observed in the experiment, named as PL5-PL6^{43,44} and PL5'-PL6' and PL7-PL10⁵⁰. Recently, some of these lines were tentatively assigned to stacking

fault-divacancy complexes.⁵¹ Hereinafter, we consider the four regular divacancy configurations (PL1-4) only.

There are several spin defects in 4H-SiC that can influence the spin dynamics of a point defect qubit. Considering the total spin momentum and the kind of the spins, we identify four groups of spin defects that we consider separately in this article: 1) Spin-1/2 nuclear spins due to paramagnetic ^{13}C (1.07%) and ^{29}Si (4.68%) isotopes, which are naturally abundant in SiC. 2) Dopants and intrinsic defects with a spin-1/2 electronic ground state are the dominant electron spin defects in SiC. Besides these two common spin defects, we consider two, more exotic categories, namely, 3) nearby divacancies as environmental spin defects, and 4) spin-3/2 silicon vacancies as environmental spin defects. While these defects have generally low concentrations ($< 10^{14} \text{ cm}^{-3}$) in high purity samples⁵², due to irradiation and ion implantation, often used to create divacancy and silicon vacancy qubits, their concentration can be considerably enhanced. For example, after irradiation and annealing, the silicon vacancy concentration can be in the 10^{16} cm^{-3} range or even more in heavily irradiated samples.⁵³

Depending on the growth process and after-growth treatments, SiC can accommodate several spin-1/2 dopants and defects in varying concentrations. In as-grown high purity SiC epilayers, the dominating impurities and defects with non-zero electron spin are: a) nitrogen substitutional defects with typical concentration of 10^{14} - 10^{15} cm^{-3} for commercial layers, 10^{13} cm^{-3} for ultra-pure epilayers⁵², 10^{14} - 10^{15} cm^{-3} for high-purity semi-insulating (HPSI) 4H-SiC.⁵⁴ It is worth mentioning that the nitrogen nucleus also possesses a spin of $I = 1$ (99.63%) that couples through an isotropic hyperfine interaction of 50.97 MHz to the electron spin.⁵⁵ b) Shallow boron defect with 10^{14} cm^{-3} concentration for commercial layers, 10^{13} cm^{-3} concentration for pure layers, and 10^{14} - 10^{15} cm^{-3} for HPSI 4H-SiC.⁵⁴ While boron also possesses a non zero nuclear spin, the spin density of the defect is localized on other neighboring atoms with low paramagnetic isotope abundance⁵⁵, thus hereinafter we neglect the hyperfine interaction for the shallow boron acceptor. c) Carbon vacancy with 10^{13} cm^{-3} in pure epilayers and 10^{15} cm^{-3} in HPSI 4H-SiC.⁵² d) Carbon antisite-vacancy (CAV) defects can be present in HPSI materials with concentration 10^{14} - 10^{15} cm^{-3} .⁵⁴ e) In p-type samples the concentration of aluminum is typically in the range of $1\text{-}5 \times 10^{18} \text{ cm}^{-3}$. The hyperfine splitting due to paramagnetic aluminum isotope is not resolved in 4H-SiC.⁵⁵

III. METHODOLOGY

In order to faithfully simulate spin relaxation processes, we utilize the method developed in Ref. [46]. In the simulations we consider a central divacancy defect interacting with its environment, i.e. a bath of spins consisting of one type of spin defects from categories 1)-4), in a central spin arrangement. Considering only one type of spins, typically the closest spin defects play the major role in thermalizing the central spin. We found that inclusion of the 32 closest defects already provides convergent results in terms of spin relaxation. The many-spin system is then divided into a cluster of subsystems which includes the central divacancy and one defect spin each, see Fig. 1 in Ref. [46]. The applied theoretical method⁴⁶ introduces an effective interaction between the subsystems in such a way that the total spin of the many-spin system is preserved throughout the simulation. This ensures reliable simulation of spin relaxation and calculation of T_1 , as demonstrated for the case of the NV center in Ref. [46]. In this article, we study ensemble averaged quantities. Therefore, in all cases an ensemble of randomly generated local spin environments is considered. In our qualitative (quantitative) study of divacancy ensembles we consider 100 (200) random spin configurations corresponding to a given defect concentration on average. The time step is set to 25 ps (20 ps), while the simulation time is set to 1 μ s (600 μ s) for the qualitative (quantitative) analysis of the relaxation processes. When the hyperfine interaction induced spin relaxation is investigated, 100 ps time step and 600 μ s simulation time are used, and ensemble averaging is carried out over 100 random configurations of a bath containing 128 nuclear spins. Increasing the number of spins is motivated by the spatial extension of the spin density of the divacancies, which is comparable with the distances of the closest spins alike to the case of point defect spins.

In our real time simulations we investigated the time dependent variation of the initial population of the divacancy spin states. At $t = 0$, the central divacancy is initialized in the $m_S = 0$ state, while the spin bath in an high temperature thermal state.

We simulate the dynamics of the coupled spin system without any additional approximation on the local Hamiltonian of the divacancy, the spin defects, and the environmental coupling of the divacancy. Intra-spin-bath interactions, on the other hand, are neglected. The spin Hamiltonian thus can be written in the form of

$$H = H_{\text{div}} + H_{\text{bath}} + H_{\text{coup}}, \quad (1)$$

where the Hamiltonian H_{div} of the divacancy consists of three terms

$$H_{\text{div}} = g_e \mu_B B_z S_z + D \left(S_z^2 - \frac{2}{3} \right) + \frac{E}{2} (S_+^2 + S_-^2), \quad (2)$$

where g_e is the electron g-factor, μ_e is the Bohr magneton, B_z is the external magnetic field parallel to the quantization axis of the central divacancy defect set by the V_C - V_{Si} defect axis, S_z is the electron spin z operator, S_+ and S_- are the electron spin ladder operators, and D and E are the zero-field splitting parameters. Due symmetry constraints the E splitting is zero for the C_{3v} symmetric hh and kk configurations, while it is non-zero for the C_{1h} symmetric kh and hk configurations. The experimental zero-field-splitting parameters used in the simulations are reported in Ref. [56]. The bath Hamiltonian and the coupling Hamiltonian depend on the spin defect considered. For nuclear spins ($I = 1/2$) the bath Hamiltonian includes the nuclear Zeeman term only

$$H_{\text{bath}}^{\text{nuc}} = - \sum_i g_{n,i} \mu_N B_z I_{z,i}, \quad (3)$$

where μ_N is the nuclear magneton, $g_{n,i}$ is the nuclear g-factor of nucleus i being either a ^{29}Si nucleus or a ^{13}C nucleus, and $I_{z,i}$ is the nuclear spin z operator of nucleus i . For a nuclear spin bath, the coupling Hamiltonian includes the hyperfine term

$$H_{\text{coup}}^{\text{nuc}} = \sum_i S A_i I_i, \quad (4)$$

where the hyperfine tensors A_i are obtained from *ab initio* supercell calculations combined with real space integration methods⁴⁶ in order to eliminate finite size effects.

The bath Hamiltonian for spin-1/2 point defects can be written as

$$H_{\text{bath}}^{\text{spin-1/2}} = \sum_i g_e \mu_B B_z S_{z,i} + S_i A_i \mathcal{I}_i, \quad (5)$$

where the first term is the Zeeman energy of the spin-1/2 bath and the second term is the leading hyperfine interaction for a considered paramagnetic defect. Here, S and \mathcal{I} are the electron spin operator vector of the environmental defect spin and the nuclear spin operator vector of a nucleus strongly coupled to the defect's electron spin through the hyperfine tensor \mathcal{A} , respectively. Based on the discussions in Sec. II, we consider only the nuclear spin of the ^{14}N of the shallow nitrogen donor in our study.

The bath Hamiltonian of environmental divacancy spins contains the Zeeman term and the zero-field-splitting terms as specified in Eq. (2). It is worth mentioning that the quantization axis of the

environmental divacancies may not be parallel to the quantization axis of the central divacancy and the external magnetic field. In the random spin bath configurations, we consider all possible arrangements.

According to Ref. [57] the bath spin Hamiltonian for the quartet silicon vacancy can be written as

$$H_{\text{bath}}^{\text{spin-3/2}} = \sum_j \left(D_{\text{VS},j} \left(\mathcal{S}_{zj}^2 - \frac{5}{4} \right) + \left[g_e \mathcal{S}_{zj} + g_{3\parallel} \frac{\mathcal{S}_{+j}^3 - \mathcal{S}_{-j}^3}{4i} \right] \mu_B B_{\parallel} \right) + \sum_j \left(g_e \mu_B \mathcal{S}_{\perp} B_{\perp} + g_{3\perp} \mu_B \frac{\{\mathcal{S}_{+j}^2, \mathcal{S}_{zj}\} B_+ - \{\mathcal{S}_{-j}^2, \mathcal{S}_{zj}\} B_-}{2i} \right) \quad (6)$$

where the higher order g-factors $g_{3\parallel}$ and $g_{3\perp}$ are measured in Ref. [57], the zero-field-splitting constant $D_{\text{VS},j}$ of the environmental silicon vacancy centers is set either to 2.6 MHz or to 35 MHz for the two possible silicon vacancy configurations⁵⁸, B_{\parallel} and B_{\perp} are the component of the magnetic field parallel and perpendicular to the C_{3v} axis of the silicon vacancy, and $B_{\pm} = B_{\perp x} \pm iB_{\perp y}$. For C_{1h} symmetric divacancy configurations, the high symmetry axis and the quantization axis of the silicon vacancy is 109.5 degree aligned to the quantization axis of the central defect and the external magnetic field.

For point defect spin environments, the coupling Hamiltonian includes dipole-dipole interaction term:

$$H_{\text{coup}}^{\text{point}} = \sum_i -\frac{\mu_0 g_e^2 \mu_B^2}{4\pi |r_{0i}|^3} (3 (S r_{0i}) (\mathcal{S}_i r_{0i}) - S \mathcal{S}_i), \quad (7)$$

where r_{0i} is the vector pointing from the position of the central divacancy to the position of spin defect i .

In Sec. IV A, we utilize our methodology to identify magnetic field values where spin bath couplings and derived relaxation processes may be resonantly enhanced due to level crossings and cross relaxation effects. In order to capture all resonances, we simulate high concentrations spin environments, that is the concentration is set to 10^{18} cm^{-3} corresponding to doped or highly irradiated samples. In our quantitative study we focus on the depopulation of the highly populated $m_S = 0$ state due to spin precession and spin flip-flops induced by a spin bath. As the luminescence of divacancies is sensitive to the population of the $m_S = 0$ state, the results presented in Sec. IV A are comparable with magnetic field dependent PL plots. The intensity of the divacancy luminescence can be estimated from our results according to the following expression

$$\mathcal{L} \approx \mathcal{L}_0 (1 - C p_{m_S=\pm 1}), \quad (8)$$

where $p_{m_S=\pm 1}$ is the population of the $m_S = \pm 1$ states, C is the optical spin contrast, and \mathcal{L}_0 is the luminescence of the bright $m_S = 0$ state.

In Sec. IV B, we study spin relaxation quantitatively, i.e. calculate the spin relaxation rate T_1^{-1} , for the most relevant cases. To simulate spin relaxation we do not include additional jump and decoherence operators with adjustable rate parameters in the Lindbladian formalism.

IV. RESULTS

A. Resonant spin bath couplings

First we study resonance effects due to the most common spin defects in SiC, i.e. nuclear spin and spin-1/2 point defects. Spin mixing curves due to ^{29}Si and ^{13}C nuclear spins exhibit a single resonance place that corresponds to ground state level anticrossing (GSLAC) of the divacancy electron spin states, as will be shown in Sec. IV B. At the magnetic field value of the GSLAC, $B_{\text{GSLAC}}(D, E) = (D - E) / g_e \mu_B$ the Zeeman shift of the $m_S = -1$ divacancy spin states compensates the zero-field-splitting. The gapless electron spin states can be efficiently mixed either with each other through the precession of the electron spins due to transverse magnetic field, or with nuclear spin states due to the hyperfine interaction. The latter effect gives rise to strong relaxation effect at B_{GSLAC} . Note that for different divacancy configurations the GSLAC resonance appears at different magnetic field values due to the different D and E values of the centers. Note also that the different divacancy configurations possess different neighboring shells, which, however, on average has minor effects on the overall strength of the mixing.

Spin-1/2 point defects, like boron, aluminum, nitrogen dopants, carbon vacancies, and CAV defects give rise to two distinct level crossings at B_{GSLAC} and $B_{\text{GSLAC}}/2$, see Fig. 1(a), that result in resonant spin relaxation, see group I and II peaks in Fig. 1(b). The GSLAC resonance is due to the precession of the divacancy spins induced by the transverse field of the spin defects. At $B_{\text{GSLAC}}/2$, the $|m_S, m_{S,i}\rangle = |0, +1/2\rangle$ and $|-1, -1/2\rangle$ states cross. Due to the dipole-dipole interaction of the neighboring paramagnetic defects, a LAC is formed at $B_{\text{GSLAC}}/2$ and efficient spin flip-flop interaction takes place. While divacancies can polarize nuclear spin at B_{GSLAC} , they can polarize spin-1/2 electron spins only at $B_{\text{GSLAC}}/2$. Note that when a strong hyperfine coupling is not expected at the spin defect site, a featureless resonance peak is observed as seen in Fig. 1(b). On the other hand, the nitrogen dopant, exhibits a strong hyperfine interaction with its abundant

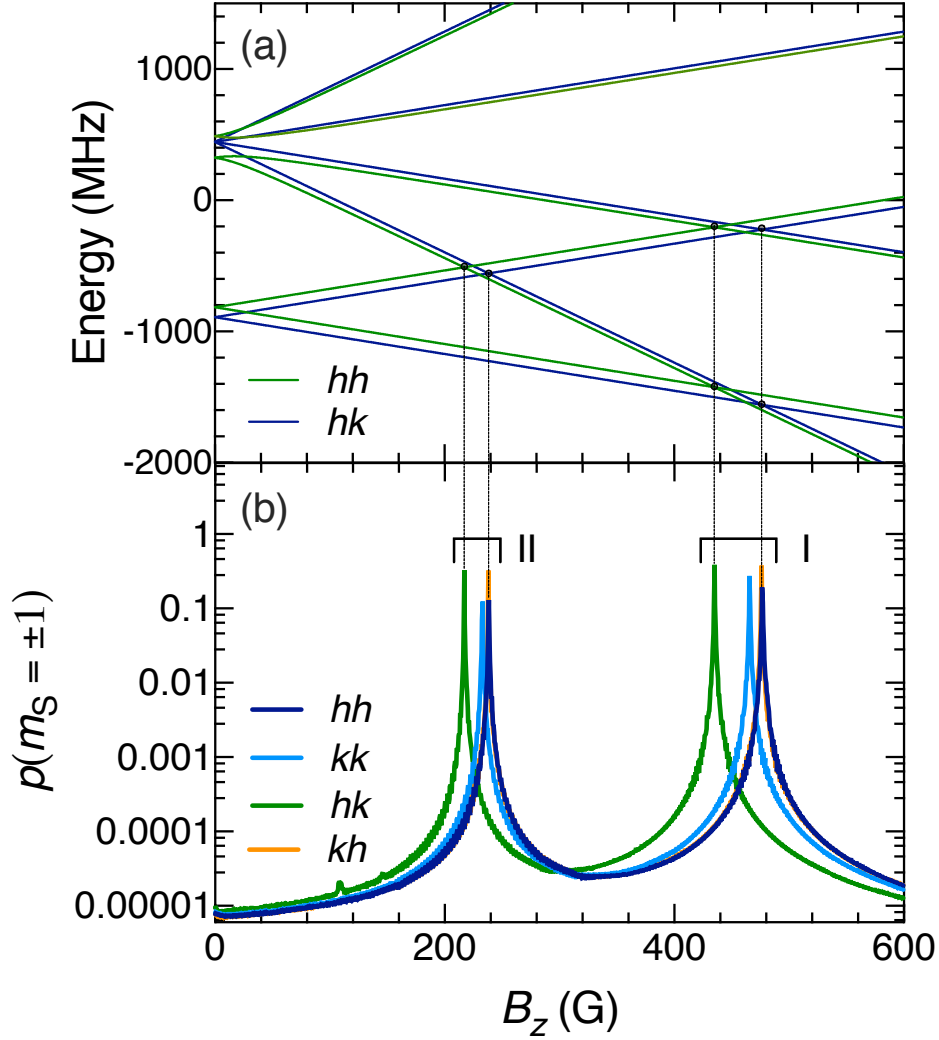


FIG. 1. a) Magnetic field dependence of the energy levels of hh (dark blue) and hk (green) divacancies coupled to a single spin-1/2 point defect. b) Population of the $m_S = \pm 1$ spin states of the hh (dark blue), kk (light blue), hk (green), and kh (amber) divacancies induced by a bath of spin-1/2 environmental defects at the concentration of 10^{18} cm^{-3} . The depicted curves show the magnetic field dependence of the population enhancement of the $m_S = \pm 1$ states of the divacancies. Each curve exhibits two resonances corresponding to $B_{\text{GSLAC}}(D, E)$ (group I) and $B_{\text{GSLAC}}(D, E)/2$ (group II), where D and E are the ZFS parameters of the corresponding divacancy qubit. In a) and b) the magnetic field is parallel to the quantization axis of the divacancy qubits in all cases. At $t = 0$, the central divacancy is initialized in the $m_S = 0$ state, while the spin bath in an high temperature thermal state.

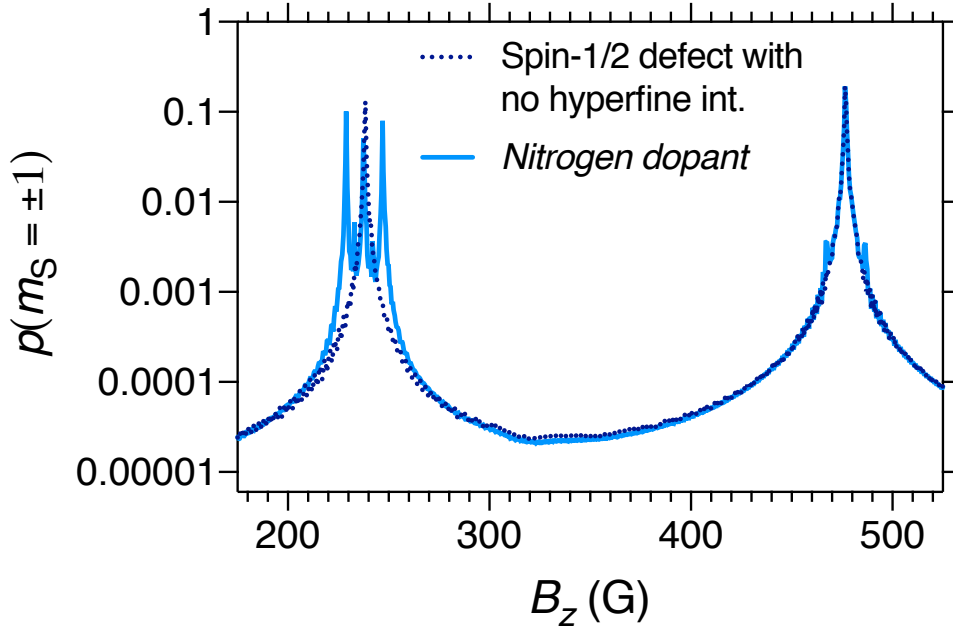


FIG. 2. Population of the $m_S = \pm 1$ spin states for the case of spin-1/2 defect with strong hyperfine interaction. Solid light blue line shows the population variation of the hh divacancy spin states due to substitutional nitrogen shallow donor. Dotted dark blue depicts population variation due to spin-1/2 electron spin defects without the hyperfine coupling. Hyperfine interaction leads to a splitting of the center peak into three peaks at $B_{\text{GSLAC}}/2$ as well as to an appearance of two satellite peaks next to the GSLAC peaks.

^{15}N nuclear spin, resulting in a fine structure, see the dashed line in Fig. 2 for the hh divacancy. The hyperfine interaction at the spin defect site leads to a splitting of the resonance peaks in group II at $B_{\text{GSLAC}}/2$ according to the nuclear spin states. In addition, two satellite peaks appear on the GSLAC resonance peak, see Fig. 2. The curves are similar to those reported for the NV center in diamond interacting with substitutional nitrogen point defects^{39,42}. However, in hexagonal SiC polytypes there is only one allowed symmetry distortion and the hyperfine interaction is dominantly isotropic⁵⁵, which leads to a less complicated spin structures at $B_{\text{GSLAC}}/2$.

More exotic couplings are possible when the divacancies interact with other divacancies or with spin-3/2 silicon vacancy centers. This may be the case in highly irradiated samples or when the sample is bombarded with positive ions creating hundreds of defects in a small volume⁵⁹. In Fig. 3, we depict the magnetic field dependence of the population of the divacancy $m_S = \pm 1$ spin states due to spin flip-flops induced by V1 and V2 silicon vacancy centers⁵⁸. The curves resemble in their main character the mixing curves of the spin-1/2 defects. It is indeed expected as the quartet

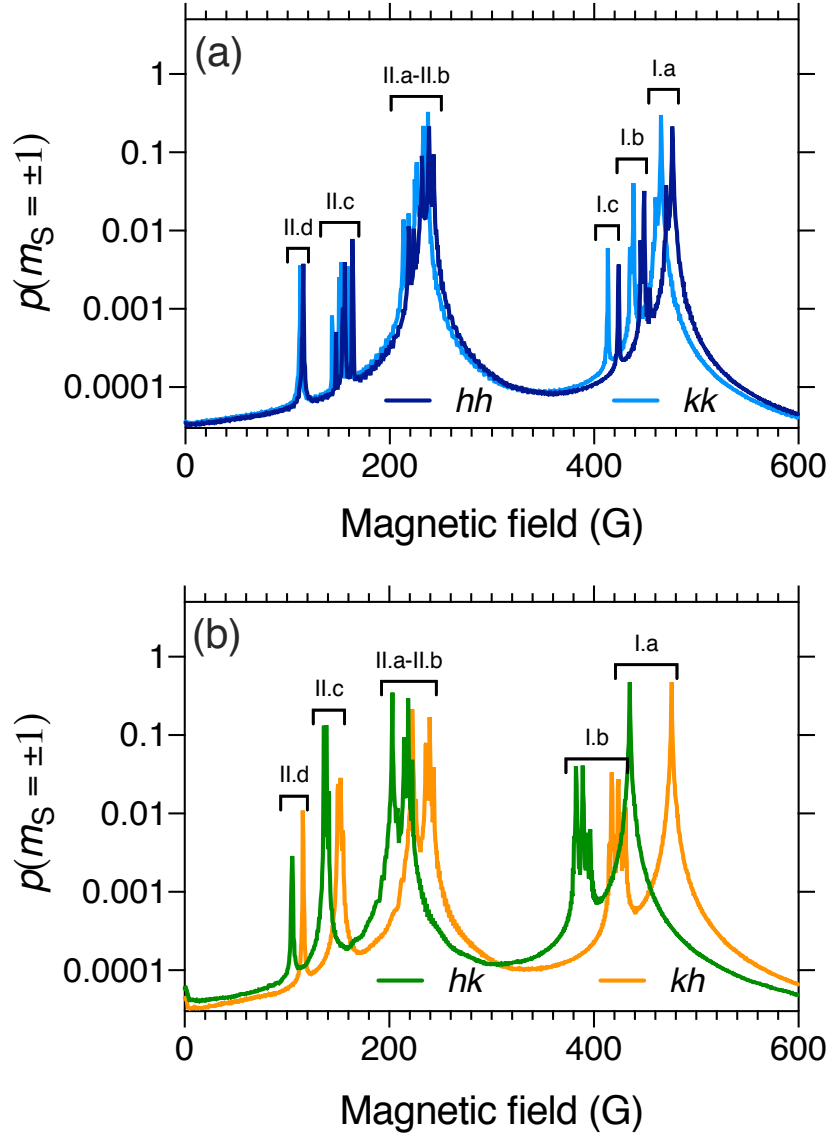


FIG. 3. Magnetic field dependence of the population of the divacancy $m_S = \pm 1$ spin states due to spin flip-flops induced by V1 and V2 silicon vacancy centers. a) and b) depict the magnetic field dependence of the spin mixing of hh and kk and hk and kh divacancy centers, respectively. In addition to the primary peaks I.a and II.a, observed for spin-1/2 defect, satellite peaks I.b, I.c, II.b, and II.c can be observed to the left of their respective primary peaks. The satellite peaks correspond to double and triple quantum jumps of environmental silicon vacancies. In a) and b) the magnetic field is parallel to the quantization axis of the divacancy qubits in all cases. At $t = 0$, the central divacancy is initialized in the $m_S = 0$ state, while the spin bath is in a high temperature thermal state.

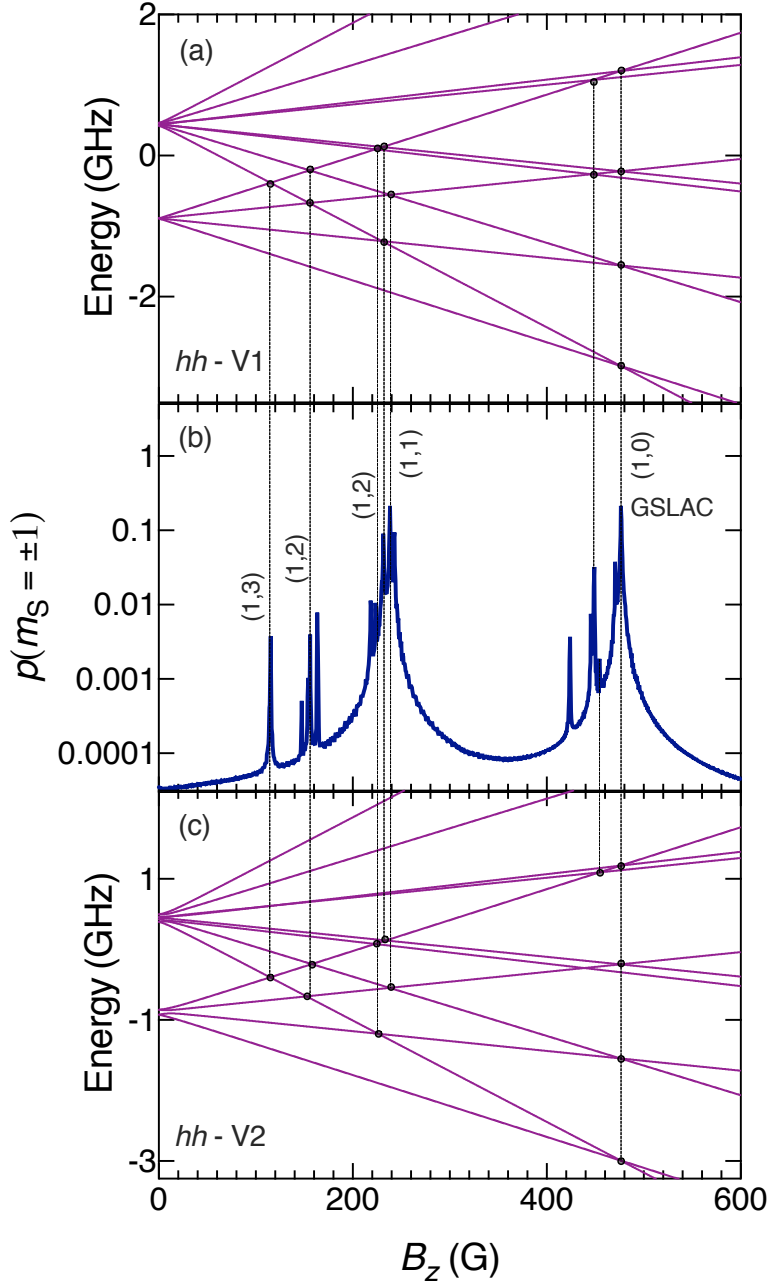


FIG. 4. Identification of resonance peaks for the hh divacancy interacting with spin-3/2 silicon vacancy centers. a) and c) show the energy levels structure of hh divacancy-V1 silicon vacancy and hh divacancy-V2 silicon vacancy two spin systems, respectively. b) depicts the derived population curve for hh divacancy. At each resonance peak, a pair of numbers in parenthesis provide the jump of the spin quantum numbers of the divacancy and silicon vacancy centers at the assigned level crossings.

spin of the silicon vacancy contains a $m_S = \{+1/2, -1/2\}$ manifold that can interact with the divacancy spin states as the spin-1/2 defect spins. Accordingly, we observe two main resonance I.a and II.a at magnetic field values B_{GSLAC} and $B_{\text{GSLAC}}/2$. In addition to these dominant peaks several satellite peaks can be observed on the left side of both primary resonances. Majority of the peaks can be connected to level crossings, see Fig. 4. To allow spin mixing at these crossings the quantum number of the silicon vacancy spin must jump either by two or by three, see Fig. 4. Note that dipole-dipole interaction does not include such Hamiltonian terms. However, higher order Zeeman terms are non-zero for quartet spin states in C_{3v} symmetry, see in Eq. (6), which in combination with the dipole-dipole interaction makes a weak mixing of the divacancy and silicon vacancy spin states possible. Peaks II.d require the triple quantum jumps, i.e. $(\Delta m_S, \Delta m_S) = (1,3)$, while peaks I.b, II.b, and II.c require double quantum jumps from the silicon vacancy spin, i.e. $(\Delta m_S, \Delta m_S) = (1,2)$.

In order to investigate the interaction between divacancy centers we studied each divacancy configuration interacting with a bath of other possible divacancies. The obtained spin polarization curves exhibit a complicated pattern which has not been seen so far, see Fig. 5. Besides the GSLAC resonance, C_{3v} symmetric configurations exhibit two other groups of resonance peaks, peaks III and IV. In order to understand the origin of these resonances, we shortly discuss the energy level structure of divacancy pairs. At zero magnetic field, the states of all divacancy pairs, irrespective to their local quantization axis, split into three manifolds, 1) the single degenerate $|m_S, m_S\rangle = |0, 0\rangle$ manifold with the lowest energy, 2) the $\{|0, \pm 1\rangle, |\pm 1, 0\rangle\}$ manifold, and C) the $\{|\pm 1, \pm 1\rangle, |\mp 1, \pm 1\rangle\}$ manifold with the highest energy, see Fig. 6. The GSLAC resonance is due to the crossing between the $|0, 0\rangle$ state and states of the $\{|0, \pm 1\rangle, |\pm 1, 0\rangle\}$ manifold. Group III peaks appear at crossings of manifolds 2) and 3), see Fig. 6. Note that spin mixing at such level crossings is only possible when divacancies with two different quantization axes are interacting. In this case the Zeeman interaction partially mixes the spin states of one of the divacancies. Combined with dipole-dipole interaction this makes spin flip-flop interaction possible at the crossings. Accordingly, peaks III.a and III.c and peak III.b in Fig. 5(a) originate from interactions with hk and kh basal plane oriented divacancy centers, respectively, see Fig. 6. Group III peaks include four peaks for basal plane oriented divacancy configurations (Fig. 5(b)), each of them corresponds to interaction with divacancies, hh , kk , hk , and kh , whose quantization axis is 109 degree aligned to the quantization axis of the considered basal plane divacancy. Group IV. peaks correspond to crossings between the states of the $\{|0, \pm 1\rangle, |\pm 1, 0\rangle\}$ manifold, see Fig. 6. As the splitting of

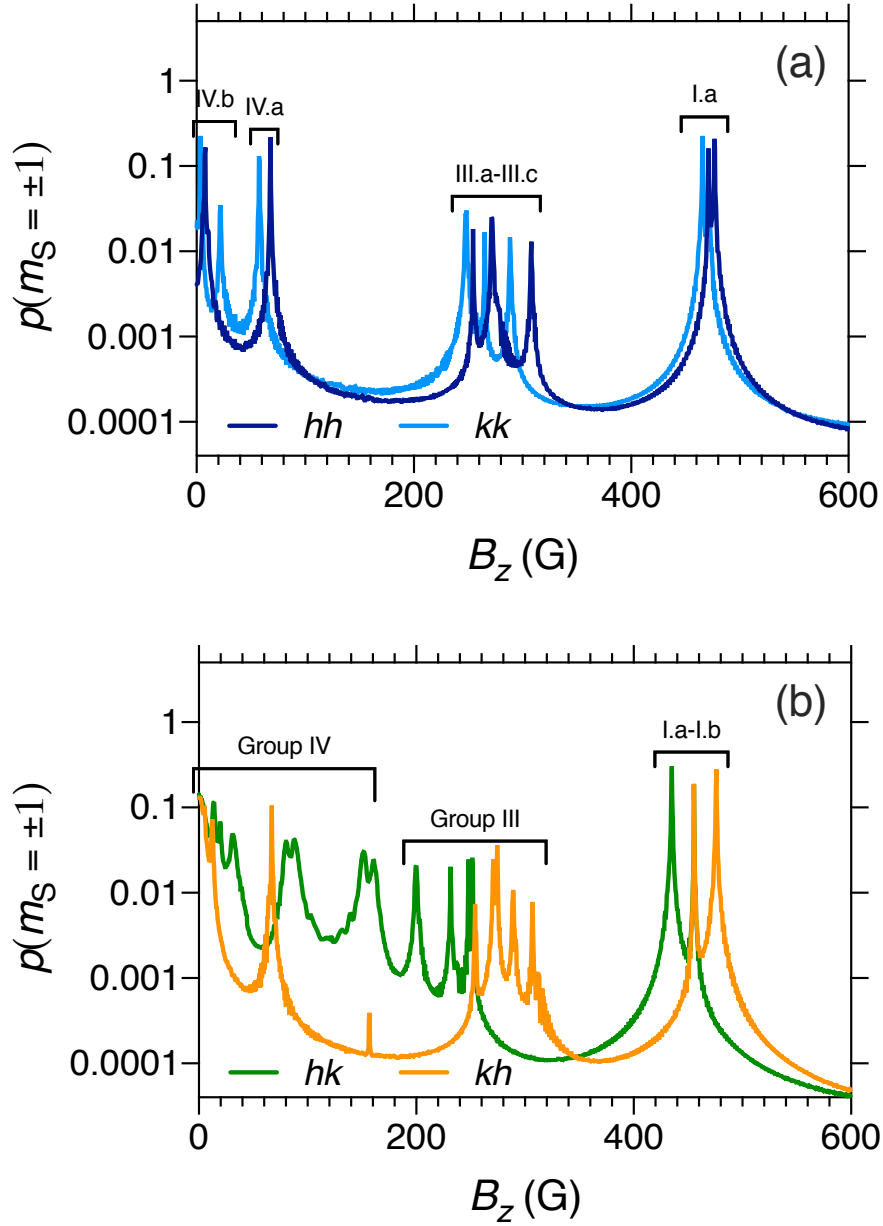


FIG. 5. Population of the $m_S = \pm 1$ spin states of divacancies interact with other divacancy spins. a) and b) show the mixing curves on a logarithmic scale of the hh and kk and the hk and kh divacancy centers, respectively. In all cases the spin bath contains all the possible divacancy configurations other than the central divacancy under consideration. In a) and b) the magnetic field is parallel to the quantization axis of the divacancy qubits in all cases. At $t = 0$, the central divacancy is initialized in the $m_S = 0$ state, while the spin bath in an high temperature thermal state.

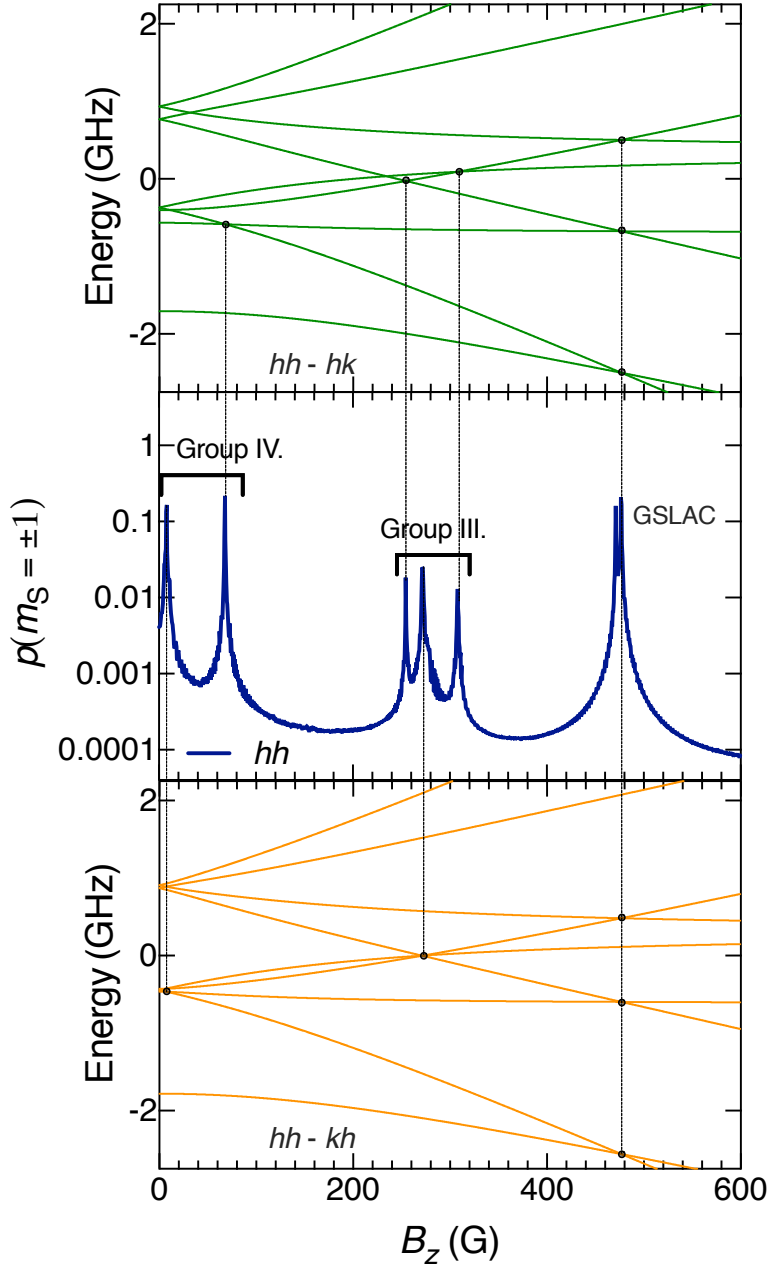


FIG. 6. Identification of resonance peaks for the hh divacancy interacting with other divacancy centers. a) and c) show the energy levels structure of hh divacancy- hk divacancy and hh divacancy- kh divacancy two spin systems, respectively. At zero magnetic field the spin states split into three well separated manifolds. b) depicts the derived spin population curve for the hh divacancy.

the states in the middle manifold is small compared with the D zero-field-splitting parameter, the resonances peaks appear at small magnetic field values in most cases. The positions of the cross-

ings largely depended on the differences of the D splittings and the values of the E splitting of the coupled divacancy centers. The ZFS parameters of the hk divacancy deviates the most from the ZFS parameters of the other configurations. Consequently, the crossing region stretches over a magnetic field interval of 175 G. Furthermore, accidental degeneracies can be observed in the energy level structure (not shown) that give rise to broad resonance peaks as can be seen in Fig. 5(b) for the hk divacancy center.

As the different spin defects give rise to different signatures, study of spin mixing can be utilized to identify the dominant spin-spin interactions in a sample. In case of single defects, spin mixing, detectable through the spin dependent luminescence of the centers, can provide valuable information on the local environment of the centers.

B. Longitudinal spin relaxation

In this section, we carry out quantitative study on the relaxation dynamics of the divacancy qubits in different spin environments and determine the magnetic field and concentration dependence the longitudinal spin relaxation rate T_1^{-1} . Here, we focus only on the most relevant spin defects in SiC, namely ^{29}Si and ^{13}C nuclear spins and spin-1/2 point defects. Figs. 7 a) and b) depict the calculated spin relaxation rate for hh divacancy qubit embedded in a nuclear spin environment and spin-1/2 point defect environment of different concentrations, respectively. Here, we note that when ^{13}C spin bath is considered the nearest neighbor sites are excluded. Comparing the ^{13}C nuclear spin environment induced spin relaxation rate with the one obtained for the NV center⁴⁶, one can notice that the paramagnetic carbon nuclei of natural abundance give rise to comparable but somewhat smaller relaxation rate for the hh divacancy in SiC. This is due to the fact that the lattice constant of SiC is larger than in diamond, thus the hyperfine interaction decreases faster within the neighboring shells. In addition, carbon atoms occupy only half of the sites in the vicinity of the defect. For example, the second neighborhood shell, that contains twelve sites with hyperfine interaction ≈ 10 MHz, is occupied by silicon atoms. This very last argument suggests that ^{29}Si paramagnetic silicon nuclei of 4.6% natural abundance have strong effect on the spin relaxation time. Indeed, according to our simulations ^{29}Si nuclear spins limit the ensemble averaged T_1 time to 100-500 ms farther away from the GSLAC resonance. We note that the spin relaxation rate of individual divacancy centers can vary over several orders of magnitude due to their distinct local environment. As can be seen in Fig. 7, the largest relaxation rate found in our ensemble is

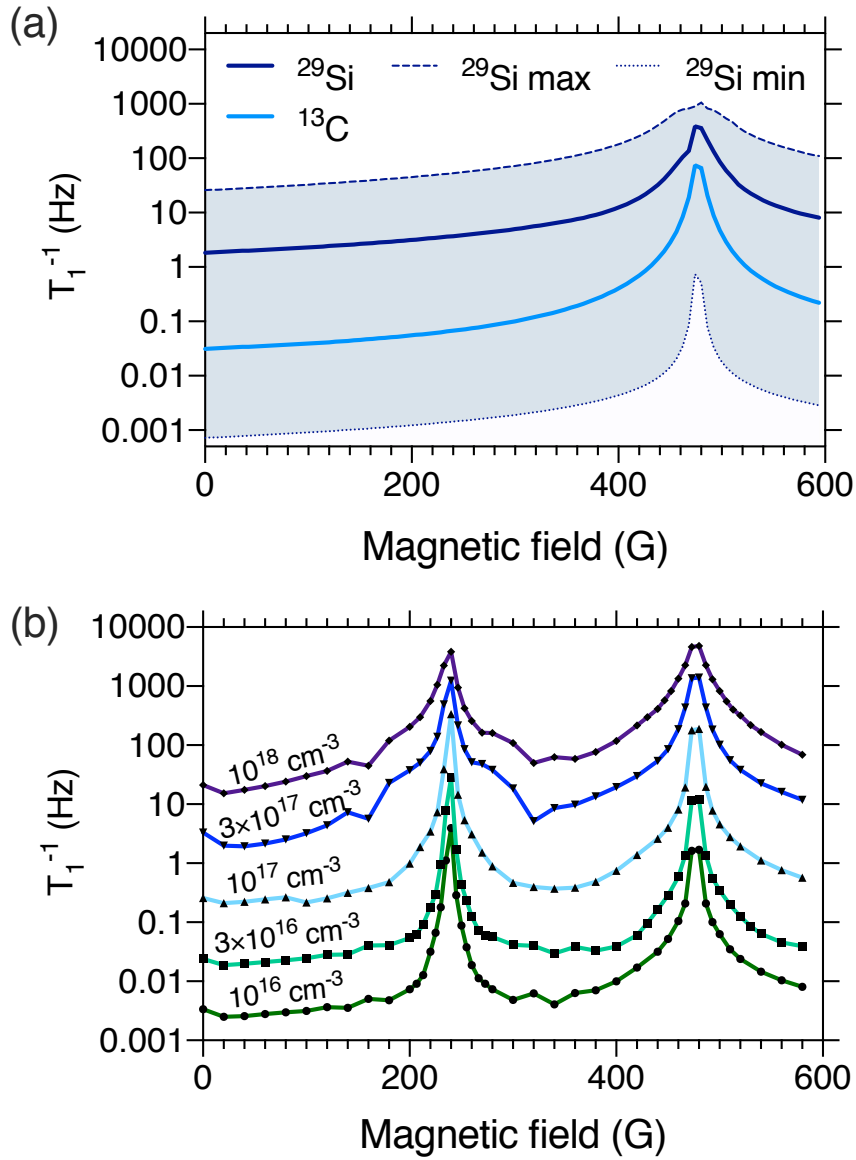


FIG. 7. Magnetic field dependence of the longitudinal spin relaxation rate T_1^{-1} due to a) nuclear spin of natural abundance and b) spin-1/2 point defects of various concentrations. a) Relaxation due to ^{29}Si (solid dark blue line) and ^{13}C (solid light blue line) nuclear spins are considered separately. When ^{13}C spin bath is considered the nearest neighbor sites are excluded. For ^{29}Si we also depict the largest (dashed dark blue line) and the smallest (dotted dark blue line) relaxation rate found in our ensemble of 100 configurations. The shaded area between these curves covers more than four orders of magnitude.

an order of magnitude larger than the average, while the smallest one is more than three orders of magnitude smaller than the average.

Comparing Figs. 7(a) and (b), one can see that, spin-1/2 point defect induced relaxation starts to dominate, except the resonance place at $B_{\text{GSLAC}}/2$, only at defect concentrations as high as $3 \times 10^{18} \text{ cm}^{-3}$. Therefore, we conclude that in samples of natural isotope abundance, ^{29}Si nuclei are the main non-thermal source of spin relaxation. In ^{29}Si isotope depleted samples, depending on their net concentration, spin-1/2 point defects may dominantly contribute to spin relaxation at low temperature. Fig. 7(b) shows the magnetic field dependence of the relaxation rate at various concentrations of spin-1/2 point defects ranging from 10^{16} cm^{-3} to 10^{18} cm^{-3} . Note that the lowest concentration considered in this study is still considered to be high in SiC, however, below this level ^{13}C nuclear spins start to dominate the relaxation dynamics.

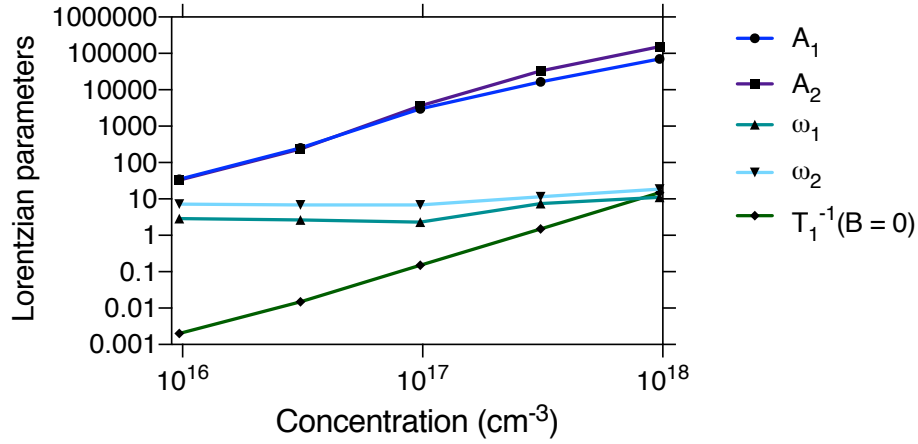


FIG. 8. Concentration dependence of the fitting parameters of Eq. (9) fitted to the simulated spin-1/2 defect concentration dependent spin relaxation rate curves in Fig 7(b).

In order to make our numerical results more accessible, we parameterize all the curves depicted in Fig. 7(b). We use a double-Lorentzian form

$$T_1^{-1}(B, C) = T_1^{-1}(0, C) + \frac{2A_1}{\pi} \frac{\omega_1}{4(B - B_{\text{GSLAC}/2})^2 + \omega_1^2} + \frac{2A_2}{\pi} \frac{\omega_2}{4(B - B_{\text{GSLAC}})^2 + \omega_2^2}, \quad (9)$$

where B is the magnetic field and C is the concentration of spin-1/2 defect. $T_1^{-1}(0, C)$, the relaxation rate at $B = 0$, A_1 , A_2 , ω_1 , and ω_2 are fitting parameters which are depicted in Fig. 8 as a function of the spin-1/2 defects concentration. In order to be able to extrapolate to concentrations that are not considered in our numerical simulations, we fitted polynomial curves to the concentration dependence of the parameters of Eq. (9), as

$$X(C) = \alpha + \beta C^n, \quad (10)$$

where X is a parameter of the double-Lorentzian curve. The simple polynomial form given in Eq. (10) fits well the curves depicted in Fig. 8. Table I provides the parameters of these polynomial fits. To obtain the relaxation rate for a particular defect concentration given in cm^{-3} unit, one can determine the corresponding Lorentzian parameters using Eq. (10) and Table I and insert them into Eq. (9). This will provide the ensemble averaged relaxation rate in Hz unit.

TABLE I. Parameters of the polynomial fits describing concentration dependence parameters of the double-Lorentzian curve fitted to the numerical results.

Parameters of the Lorentzians	α	β	n
A_1	0	1.75×10^{-25}	1.65
A_2	0	1.23×10^{-29}	1.9
ω_1	2.87	1.6×10^{-15}	0.875
ω_2	6.89	1.23×10^{-17}	1
$T_1^{-1}(B = 0)$	0	1.6×10^{-35}	2

Considering the concentration dependence of the spin-1/2 point defects induced relaxation rate at zero magnetic field, we obtain a simple quadratic concentration dependence of the relaxation rate,

$$T_1^{-1}(B = 0, C) = \beta C^2 \quad (11)$$

where $\beta = 1.6 \times 10^{-35} \text{ Hz/cm}^{-6}$. Note that the quadratic dependence given by Eq. (11) differs from the earlier experimental reports³⁷ observing linear dependence on the concentration. We attribute the difference to the uncertainties in the concentration and relaxation rate measurements and to the smaller concentration interval considered in the experiment.

V. CONCLUSIONS

In summary, in this article we have reported a systematic study of the spin relaxation dynamics of divacancy qubits in 4H-SiC. First, we examined the magnetic field dependence of the spin mixing induced by various spins in the local environment of divacancy qubits. We demonstrated that other neighboring divacancy centers and the spin-3/2 silicon vacancy centers give rise to a rich relaxation patterns with multiple of relaxation peaks of various amplitudes. The distinct relaxation pattern of the different spin defects allows one to identify and study the local environments of

a single divacancy qubit. Applications, such as dynamic nuclear polarization, microwave free sensing, and spin relaxation spectroscopy, that utilize LAC and cross relaxation phenomena are yet to be explored in SiC.

Based on our results one can identify magnetic field values where spin relaxation is minimal in a sample of given spin defect concentrations. In high purity samples with natural abundance of paramagnetic isotopes one needs to avoid the GSLAC region, from 400-550 G as well as the interval of 200-300 G where spin-1/2 defect, such as carbon vacancies, carbon antisite-vacancy pairs, and dopants can limit the T_1 time. When the sample is irradiated, and silicon vacancy and divacancy defects are expected in considerable amounts, a magnetic field value in the interval of 300-340 G can be an optimal choice. Alternatively, one may set magnetic field values considerably larger than B_{GSLAC} .

Moreover, we have simulated the magnetic field and concentration dependences of the spin relaxation time T_1 for the most relevant spin defects in SiC. We have shown that in high purity samples the dominant non-thermal contribution to spin relaxation comes from the ^{29}Si nuclear spin bath, that maximizes the ensemble averaged T_1 time at 100 ms at low temperature far away from the GSLAC resonance. For configurations of adjacent nuclear spins the relaxation time may reduce to 40 ms at zero magnetic field that is shorter than the coherence time of 64 ms reported in Ref. [24]. In such cases spin relaxation is a major limiting factor. ^{29}Si depleted samples on the other hand may exhibit two orders of magnitude longer T_1 time on average when ^{13}C spins are the dominant spin defects in the sample.

Dipolar spin relaxation due to spin-1/2 defects may be significant in integrated quantum devices applying doping at the qubit site and for near surface divacancy qubits. Here, we provided simple analytical formulas with Lorentzian curves approximating the resonance peaks obtained in our quantitative numerical study that can be utilized to estimate T_1 in a given sample of known spin defect concentration. In addition, our theoretical results can be used to analyze the measured T_1 to estimate the local spin defect concentration of an ensemble or a single divacancy qubits.

ACKNOWLEDGMENTS

We acknowledge support from the Knut and Alice Wallenberg Foundation through WBSQD2 project (Grant No. 2018.0071). Support from the Swedish Government Strategic Research Area SeRC and the Swedish Government Strategic Research Area in Materials Science on Functional

Materials at Linkping University (Faculty Grant SFO-Mat-LiU No. 2009 00971) is gratefully acknowledged. VI acknowledges the support from the MTA Premium Postdoctoral Research Program, the Hungarian NKFIH grants No. KKP129866 of the National Excellence Program of Quantum-coherent materials project, and the NKFIH through the National Quantum Technology Program (Grant No. 2017-1.2.1-NKP-2017-00001) and the Quantum Information National Laboratory sponsored by Ministry of Innovation and Technology of Hungary. N. T. S. acknowledges the support from the Swedish Research Council (Grant No. VR 2016-04068), the EU H2020 project QuanTELCO (Grant No. 862721). The calculations were performed on resources provided by the Swedish National Infrastructure for Computing (SNIC) at the National Supercomputer Centre (NSC).

* ivady.viktor@wigner.hu

- ¹ L. du Preez, Ph.D. thesis, University of Witwatersrand (1965).
- ² J. Wrachtrup and F. Jelezko, *Journal of Physics-Condensed Matter* **18**, S807 (2006).
- ³ J. R. Maze, A. Gali, E. Togan, Y. Chu, A. Trifonov, E. Kaxiras, and M. D. Lukin, *New Journal of Physics* **13**, 025025 (2011).
- ⁴ M. W. Doherty, N. B. Manson, P. Delaney, F. Jelezko, J. Wrachtrup, and L. C. Hollenberg, *Physics Reports* **528**, 1 (2013).
- ⁵ G. Balasubramanian, I. Y. Chan, R. Kolesov, M. Al-Hmoud, J. Tisler, C. Shin, C. Kim, A. Wojcik, P. R. Hemmer, A. Krueger, T. Hanke, A. Leitenstorfer, R. Bratschitsch, F. Jelezko, and J. Wrachtrup, *Nature* **455**, 648 (2008).
- ⁶ J. Taylor, P. Cappellaro, L. Childress, L. Jiang, D. Budker, P. Hemmer, A. Yacoby, R. Walsworth, and M. Lukin, *Nat. Phys.* **4**, 810 (2008).
- ⁷ G. Kucsko, P. C. Maurer, N. Y. Yao, M. Kubo, H. J. Noh, P. K. Lo, H. Park, and M. D. Lukin, *Nature* **500**, 54 (2013).
- ⁸ T. Plakhotnik, M. W. Doherty, J. H. Cole, R. Chapman, and N. B. Manson, *Nano Letters* **14**, 4989 (2014).
- ⁹ R. Schirhagl, K. Chang, M. Loretz, and C. L. Degen, *Annual Review of Physical Chemistry* **65**, 83 (2014), <https://doi.org/10.1146/annurev-physchem-040513-103659>.
- ¹⁰ C. L. Degen, F. Reinhard, and P. Cappellaro, *Rev. Mod. Phys.* **89**, 035002 (2017).

- ¹¹ D. R. Glenn, D. B. Bucher, J. Lee, M. D. Lukin, H. Park, and R. L. Walsworth, *Nature* **555**, 351 (2018).
- ¹² S. Schmitt, T. Gefen, F. M. Strner, T. Unden, G. Wolff, C. Mller, J. Scheuer, B. Naydenov, M. Markham, S. Pezzagna, J. Meijer, I. Schwarz, M. Plenio, A. Retzker, L. P. McGuinness, and F. Jelezko, *Science* **356**, 832 (2017).
- ¹³ H. Bernien, B. Hensen, W. Pfaff, G. Koolstra, M. S. Blok, L. Robledo, T. H. Taminiau, M. Markham, D. J. Twitchen, L. Childress, and R. Hanson, *Nature* **497**, 86 (2013).
- ¹⁴ W. Pfaff, B. J. Hensen, H. Bernien, S. B. v. Dam, M. S. Blok, T. H. Taminiau, M. J. Tiggelman, R. N. Schouten, M. Markham, D. J. Twitchen, and R. Hanson, *Science* **345**, 532 (2014).
- ¹⁵ S. Wehner, D. Elkouss, and R. Hanson, *Science* **362** (2018), 10.1126/science.aam9288.
- ¹⁶ J. R. Weber, W. F. Koehl, J. B. Varley, A. Janotti, B. B. Buckley, C. G. Van de Walle, and D. D. Awschalom, *PNAS* **107**, 8513 (2010).
- ¹⁷ G. Kurizki, P. Bertet, Y. Kubo, K. Mølmer, D. Petrosyan, P. Rabl, and J. Schmiedmayer, *Proceedings of the National Academy of Sciences* **112**, 3866 (2015), <https://www.pnas.org/content/112/13/3866.full.pdf>.
- ¹⁸ J. Zhang, S. S. Hegde, and D. Suter, *Phys. Rev. Lett.* **125**, 030501 (2020).
- ¹⁹ W. F. Koehl, B. B. Buckley, F. J. Heremans, G. Calusine, and D. D. Awschalom, *Nature* **479**, 84 (2011).
- ²⁰ D. J. Christle, A. L. Falk, P. Andrich, P. V. Klimov, J. U. Hassan, N. T. Son, E. Janzén, T. Ohshima, and D. D. Awschalom, *Nat. Mater.* **14**, 160 (2015).
- ²¹ N. T. Son, P. Carlsson, J. ul Hassan, E. Janzén, T. Umeda, J. Isoya, A. Gali, M. Bockstedte, N. Morishita, T. Ohshima, and H. Itoh, *Phys. Rev. Lett.* **96**, 055501 (2006).
- ²² V. A. Soltamov, A. A. Soltamova, P. G. Baranov, and I. I. Proskuryakov, *Phys. Rev. Lett.* **108**, 226402 (2012).
- ²³ M. Widmann, S.-Y. Lee, T. Rendler, N. T. Son, H. Fedder, S. Paik, L.-P. Yang, N. Zhao, S. Yang, I. Booker, A. Denisenko, M. Jamali, S. A. Momenzadeh, I. Gerhardt, T. Ohshima, A. Gali, E. Janzén, and J. Wrachtrup, *Nat. Mater.* **14**, 164 (2015).
- ²⁴ K. C. Miao, J. P. Blanton, C. P. Anderson, A. Bourassa, A. L. Crook, G. Wolfowicz, H. Abe, T. Ohshima, and D. D. Awschalom, *Science* **369**, 1493 (2020).
- ²⁵ D. J. Christle, P. V. Klimov, C. F. de las Casas, K. Szász, V. Ivády, V. Jokubavicius, J. Ul Hassan, M. Syväjärvi, W. F. Koehl, T. Ohshima, N. T. Son, E. Janzén, A. Gali, and D. D. Awschalom, *Phys. Rev. X* **7**, 021046 (2017).

- ²⁶ A. L. Falk, P. V. Klimov, V. Ivády, K. Szász, D. J. Christle, W. F. Koehl, A. Gali, and D. D. Awschalom, *Phys. Rev. Lett.* **114**, 247603 (2015).
- ²⁷ A. Bourassa, C. P. Anderson, K. C. Miao, M. Onizhuk, H. Ma, A. L. Crook, H. Abe, J. Ul-Hassan, T. Ohshima, N. T. Son, G. Galli, and D. D. Awschalom, *Nature Materials* **19**, 1319 (2020).
- ²⁸ Q. Li, J.-F. Wang, F.-F. Yan, J.-Y. Zhou, H.-F. Wang, H. Liu, L.-P. Guo, X. Zhou, A. Gali, Z.-H. Liu, Z.-Q. Wang, K. Sun, G.-P. Guo, J.-S. Tang, J.-S. Xu, C.-F. Li, and G.-C. Guo, arXiv:2005.07876 (2020).
- ²⁹ S. J. Whiteley, G. Wolfowicz, C. P. Anderson, A. Bourassa, H. Ma, M. Ye, G. Koolstra, K. J. Satzinger, M. V. Holt, F. J. Heremans, A. N. Cleland, D. I. Schuster, G. Galli, and D. D. Awschalom, *Nature Physics* **15**, 490 (2019).
- ³⁰ C. P. Anderson, A. Bourassa, K. C. Miao, G. Wolfowicz, P. J. Mintun, A. L. Crook, H. Abe, J. U. Hassan, N. T. Son, T. Ohshima, and D. D. Awschalom, *Science* **366**, 1225 (2019).
- ³¹ N. T. Son, C. P. Anderson, A. Bourassa, K. C. Miao, C. Babin, M. Widmann, M. Niethammer, J. Ul Hassan, N. Morioka, I. G. Ivanov, F. Kaiser, J. Wrachtrup, and D. D. Awschalom, *Applied Physics Letters* **116**, 190501 (2020).
- ³² L. M. Pham, N. Bar-Gill, C. Belthangady, D. Le Sage, P. Cappellaro, M. D. Lukin, A. Yacoby, and R. L. Walsworth, *Physical Review B* **86**, 045214 (2012).
- ³³ N. Bar-Gill, L. M. Pham, A. Jarmola, D. Budker, and R. L. Walsworth, *Nature Communications* **4**, 1743 (2013).
- ³⁴ Y. Romach, C. Müller, T. Uden, L. J. Rogers, T. Isoda, K. M. Itoh, M. Markham, A. Stacey, J. Meijer, S. Pezzagna, B. Naydenov, L. P. McGuinness, N. Bar-Gill, and F. Jelezko, *Phys. Rev. Lett.* **114**, 017601 (2015).
- ³⁵ J. F. Barry, J. M. Schloss, E. Bauch, M. J. Turner, C. A. Hart, L. M. Pham, and R. L. Walsworth, *Reviews of Modern Physics* **92**, 015004 (2020).
- ³⁶ S. Takahashi, R. Hanson, J. van Tol, M. S. Sherwin, and D. D. Awschalom, *Physical Review Letters* **101**, 047601 (2008).
- ³⁷ A. Jarmola, V. M. Acosta, K. Jensen, S. Chemerisov, and D. Budker, *Physical Review Letters* **108**, 197601 (2012).
- ³⁸ H.-J. Wang, C. S. Shin, S. J. Seltzer, C. E. Avalos, A. Pines, and V. S. Bajaj, *Nature Communications* **5**, 4135 (2014).
- ³⁹ A. Wickenbrock, H. Zheng, L. Bougas, N. Leefer, S. Afach, A. Jarmola, V. M. Acosta, and D. Budker, *Applied Physics Letters* **109**, 053505 (2016), <https://doi.org/10.1063/1.4960171>.

- ⁴⁰ J. D. A. Wood, D. A. Broadway, L. T. Hall, A. Stacey, D. A. Simpson, J.-P. Tetienne, and L. C. L. Hollenberg, *Phys. Rev. B* **94**, 155402 (2016).
- ⁴¹ J. D. A. Wood, J.-P. Tetienne, D. A. Broadway, L. T. Hall, D. A. Simpson, A. Stacey, and L. C. L. Hollenberg, *Nature Communications* **8**, 15950 (2017).
- ⁴² V. Ivády, H. Zheng, A. Wickenbrock, L. Bougas, G. Chatzidrosos, K. Nakamura, H. Sumiya, T. Ohshima, J. Isoya, D. Budker, I. A. Abrikosov, and A. Gali, arXiv:2006.05085 [cond-mat] (2020).
- ⁴³ W. F. Koehl, B. B. Buckley, F. J. Heremans, G. Calusine, and D. D. Awschalom, *Nature* **479**, 84 (2011).
- ⁴⁴ A. L. Falk, B. B. Buckley, G. Calusine, W. F. Koehl, V. V. Dobrovitski, A. Politi, C. A. Zorman, P. X.-L. Feng, and D. D. Awschalom, *Nature Communications* **4**, 1819 (2013).
- ⁴⁵ F.-F. Yan, A.-L. Yi, J.-F. Wang, Q. Li, P. Yu, J.-X. Zhang, A. Gali, Y. Wang, J.-S. Xu, X. Ou, C.-F. Li, and G.-C. Guo, *npj Quantum Information* **6**, 1 (2020).
- ⁴⁶ V. Ivády, *Phys. Rev. B* **101**, 155203 (2020).
- ⁴⁷ T. Astner, J. Gugler, A. Angerer, S. Wald, S. Putz, N. J. Mauser, M. Trupke, H. Sumiya, S. Onoda, J. Isoya, J. Schmiedmayer, P. Mohn, and J. Majer, *Nature Materials* **17**, 313 (2018).
- ⁴⁸ S. Kawanishi and T. Mizoguchi, *Journal of Applied Physics* **119**, 175101 (2016).
- ⁴⁹ J. Davidsson, V. Ivády, R. Armiento, N. T. Son, A. Gali, and I. A. Abrikosov, *New Journal of Physics* **20**, 023035 (2018).
- ⁵⁰ B. Magnusson, N. T. Son, A. Csóré, A. Gällström, T. Ohshima, A. Gali, and I. G. Ivanov, *Phys. Rev. B* **98**, 195202 (2018).
- ⁵¹ V. Ivády, J. Davidsson, N. Deegan, A. L. Falk, P. V. Klimov, S. J. Whiteley, S. O. Hruszkewycz, M. V. Holt, F. J. Heremans, N. T. Son, D. D. Awschalom, I. A. Abrikosov, and A. Gali, *Nature Communications* **10**, 5607 (2019).
- ⁵² R. Nagy, M. Niethammer, M. Widmann, Y.-C. Chen, P. Udvarhelyi, C. Bonato, J. U. Hassan, R. Karhu, I. G. Ivanov, N. T. Son, J. R. Maze, T. Ohshima, . O. Soykal, . Gali, S.-Y. Lee, F. Kaiser, and J. Wrachtrup, *Nature Communications* **10**, 1954 (2019).
- ⁵³ C. Kasper, D. Klenkert, Z. Shang, D. Simin, A. Gottscholl, A. Sperlich, H. Kraus, C. Schneider, S. Zhou, M. Trupke, W. Kada, T. Ohshima, V. Dyakonov, and G. V. Astakhov, *Physical Review Applied* **13**, 044054 (2020).
- ⁵⁴ N. T. Son, P. Carlsson, J. ul Hassan, B. Magnusson, and E. Janzén, *Phys. Rev. B* **75**, 155204 (2007).
- ⁵⁵ S. Greulich-Weber, *physica status solidi (a)* **162**, 95 (1997).

- ⁵⁶ A. L. Falk, B. B. Buckley, G. Calusine, W. F. Koehl, V. V. Dobrovitski, A. Politi, C. A. Zorman, P. X.-L. Feng, and D. D. Awschalom, *Nat. Commun.* **4**, 1819.
- ⁵⁷ D. Simin, V. A. Soltamov, A. V. Poshakinskiy, A. N. Anisimov, R. A. Babunts, D. O. Tolmachev, E. N. Mokhov, M. Trupke, S. A. Tarasenko, A. Sperlich, P. G. Baranov, V. Dyakonov, and G. V. Astakhov, *Phys. Rev. X* **6**, 031014 (2016).
- ⁵⁸ V. Ivády, J. Davidsson, N. T. Son, T. Ohshima, I. A. Abrikosov, and A. Gali, *Phys. Rev. B* **96**, 161114 (2017).
- ⁵⁹ R. Kuate Defo, X. Zhang, D. Bracher, G. Kim, E. Hu, and E. Kaxiras, *Phys. Rev. B* **98**, 104103 (2018).